



Sequential electrocatalysis by single molybdenum atoms/clusters doped on carbon nanotubes for removing organic contaminants from wastewater

Chencheng Dong^a, Zhi-Qiang Wang^b, Chao Yang^a, Xiaomeng Hu^a, Pei Wang^a,
Xue-Qing Gong^b, Lin Lin^{c,*}, Xiao-yan Li^{a,c,**}

^a Department of Civil Engineering, The University of Hong Kong, Pokfulam, Hong Kong, China

^b Key Laboratory for Advanced Materials, Centre for Computational Chemistry and Research Institute of Industrial Catalysis, School of Chemistry and Molecular Engineering, East China University of Science and Technology, 130 Meilong Road, Shanghai 200237, China

^c Institute of Environment and Ecology, Tsinghua Shenzhen International Graduate School, Tsinghua University, Shenzhen, China

ARTICLE INFO

Keywords:

Oxygen reduction reaction
Electro-Fenton
Single atomic catalysts
Hydroxyl radicals
Ibuprofen

ABSTRACT

Oxygen reduction reaction (ORR) can realize the goal of in-situ H₂O₂ generation. A suitable catalyst ensures a proper binding strength between the electrocatalyst and the intermediate (i.e., *OOH), thereby avoiding the 4-electron ORR process and H₂O production. Herein, we demonstrate that single molybdenum (Mo) atoms/clusters doped on carbon nanotubes can effectively alter the ORR pathway to generate H₂O₂; meanwhile, the established sequential ORR system for H₂O₂ production can tandemly remove ibuprofen (IBU) and other organic contaminants from water and wastewater. The results reveal that single atomic Mo clusters preferentially acted as the active sites that are merely required to overcome 0.11 eV downhill to form *OOH. Surprisingly, this tandemly constructed ORR with in-situ generated H₂O₂ performed better than the in-vitro H₂O₂ system. These findings offer a promising solution to reduce the costs related to the production and transportation of H₂O₂ for various applications, including the oxidation and removal of emerging organic contaminants from water and wastewater.

1. Introduction

Advanced oxidation processes (AOPs) are regarded as promising and dependable technologies for wastewater treatment plants (WWTPs). The generated hydroxyl radicals (•OH) facilitate the unselective oxidation of persistent organic pollutants at high reaction rates, making AOPs particularly effective for water pollution control applications [1–4]. Typically, hydrogen peroxide (H₂O₂) is an essential oxidant for AOPs; however, its storage and transportation present challenges for WWTPs. Thus, scientists have sought to use oxygen (O₂) as an alternative oxidant for AOPs, given its abundance and low cost as a resource on earth. Technically speaking, the oxygen-derived H₂O₂ concerns oxygen reduction reaction (ORR) in an electrochemical system. Specifically, O₂ would be reduced to H₂O₂ and H₂O via a 2-electron or 4-electron pathway [3], as shown in Eq. (1) and Eq. (2), respectively.



Recently, direct H₂O₂ production via ORR (i.e., electro-Fenton process) by carbonaceous nanomaterials-based catalysts has been increasingly studied, for instance, carbon tube, graphene, graphitic carbon nitride, etc. [5,6]. Nonetheless, the low H₂O₂ selectivity and yield can hinder the performance of metal-free materials, which is not advantageous for the tandem in-situ generation of H₂O₂ for the degradation of organic pollutants. The critical aspect in this context is to avoid the 4-electron process, thereby enhancing H₂O₂ yield and selectivity. Since Zhang et al. [7] found the fundamentals of single atomic catalysts (SACs), SACs have garnered significant interest in the fields of energy and environment. This is largely due to their tunable coordination structure, adjustable metal centers, electronic structure, and high porosity of the substrate. Thus, in view of the multi-electron process and sluggish kinetics of ORR, proper and effective catalysts should be fabricated to enhance ORR and electro-Fenton process efficiently and selectively [8]. In principle, the electronic structure of the catalyst may be altered by the following three means: (1) tuning the coordination structure and electronic structure of the metal centers, (2) optimizing

* Corresponding author.

** Corresponding author at: Department of Civil Engineering, The University of Hong Kong, Pokfulam, Hong Kong, China.

E-mail addresses: linlin00@sz.tsinghua.edu.cn (L. Lin), xlia@hku.hk (X.-y. Li).

<https://doi.org/10.1016/j.apcatb.2023.123060>

Received 28 March 2023; Received in revised form 28 June 2023; Accepted 28 June 2023

Available online 29 June 2023

0926-3373/© 2023 Elsevier B.V. All rights reserved.

the morphology and electronic structure of the conductive substrate, and (3) increasing the total number of metal centers [9]. However, effectively controlling the ORR pathway to produce H_2O_2 remains a challenging task. Specifically, the critical factor of improving the activity and selectivity for an ideal electrocatalyst is the binding strength between the electrocatalyst and the intermediates, which should be neither too strong nor too weak [10]. For example, Jiang et al. [11] prepared the Fe-C-O catalyst as an efficient H_2O_2 catalyst, with a low onset of 0.822 V versus the reversible hydrogen electrode and a high H_2O_2 selectivity of above 95% in both alkaline and neutral pH conditions. Adjusting the local coordination environment of SACs is believed to offer a promising opportunity to tailor the electronic structure of the catalytic sites, thereby altering ORR pathways and potentially improving the electro-Fenton (EF) performance. Nonetheless, the EF process mainly focuses on the use of ferrous (Fe^{2+}) or ferric ions (Fe^{3+}) for the catalysts. Given that element molybdenum (Mo) has been widely explored with the discovery of MoS_2 acting as a co-catalyst in the conventional Fenton process [4], a series of Mo-based catalysts have been developed for AOPs. Mo-based Fenton process has been reported for wastewater treatment [12], bacterial disinfection [13], and reduction and removal of heavy ions [14], while its low Mo leaching rate can well meet the standard of wastewater discharge. Moreover, compared to Fe^{2+} and Fe^{3+} , Mo ions are not readily to form sludge. However, limited research has been conducted on its potential application in ORR for the tandem EF process.

Inspired by this concept, we have developed a feasible, solvent-free, and environmentally friendly method to synthesize atomically dispersed Mo atoms/clusters doped on carbon nanotubes, successfully altering the carbon matrix and metal center coordination of the catalyst for the optimized electronic structure of the carbon support and increased number of metal centers. The as-prepared catalyst was employed as the cathode material in an ORR tandem EF process for the continuous removal of organic contaminants. Specifically, 98% of ibuprofen (IBU) was removed within 30 min. The external addition of O_2 and the proportion of O_2 produced from the anode play crucial roles in ORR for H_2O_2 production. The doped single Mo atoms/clusters effectively impede the 4-electron process and decompose H_2O_2 into hydroxyl radicals (i.e., heterogeneous Fenton). Density functional theory (DFT) calculations demonstrate that single atomic Mo clusters more readily adsorb the intermediate ($^*\text{OOH}$) to form H_2O_2 . This research work is expected to underpin the understanding and development of the electro-Fenton process for AOPs in wastewater treatment.

2. Experimental section

2.1. Chemicals and Reagents. All the chemicals and reagents were used without further purification

Ethanol (EtOH, Aladdin, 99.7%), multi-walled carbon nanotubes (MWCNTs) (C, 99.9%, Macklin), hydrogen peroxide (H_2O_2 , Aladdin, 30 wt%), deionized water, sodium hydroxide (NaOH, Sigma-Aldrich, 99%), ammonium heptamolybdate tetrahydrate ($(\text{NH}_4)_6\text{Mo}_7\text{O}_{24}\cdot 4\text{H}_2\text{O}$, Sigma-Aldrich, 99%), Nafion solution (Sigma-Aldrich, 99%), 5, 5-Dimethyl-1-Pyrrolidine-N-oxide (DMPO, Aladdin, 98%), ibuprofen ($\text{C}_{13}\text{H}_{18}\text{O}_2$, Sigma-Aldrich, 99%), benzophenone-3 ($\text{C}_{14}\text{H}_{12}\text{O}_3$, Alfa Aesar, 98%), carbamazepine ($\text{C}_{15}\text{H}_{12}\text{N}_2\text{O}$, Sigma-Aldrich, 99%), isopropanol ($\text{C}_3\text{H}_8\text{O}$, Sigma-Aldrich, 99%), p-Benzoquinone ($\text{C}_6\text{H}_4\text{O}_2$, Acros organic, 99%), tryptophan ($\text{C}_{11}\text{H}_{12}\text{N}_2\text{O}_2$, Sigma-Aldrich, 99%), orthophosphoric acid (H_3PO_4 , Sigma-Aldrich, 85%), acetonitrile (HPLC grade, Sigma-Aldrich, 99.9%), methanol (CH_3OH , Merck, 99.9%). All solutions were prepared from ultrapure water produced by the Lakeshore group ultrapure water system.

2.2. Preparation of single Mo atoms/clusters doped carbon nanotube

100 mg $(\text{NH}_4)_6\text{Mo}_7\text{O}_{24}\cdot 0.4\text{H}_2\text{O}$ was mixed with 500 mg carbon

nanotube, followed by calcined at 800°C ($5^\circ\text{C}/\text{min}$) under Argon (Ar) flow for another 4 h. The 25 Mo-carbon tube, 50 Mo-carbon tube, 75 Mo-carbon tube, 100 Mo-carbon tube, 150 Mo-carbon tube, and 200 Mo-carbon tube can be obtained by tuning the amount of Mo precursors (i.e., $(\text{NH}_4)_6\text{Mo}_7\text{O}_{24}\cdot 4\text{H}_2\text{O}$) at 25 mg, 50 mg, 75 mg, 100 mg, 150 mg, and 200 mg, respectively.

2.3. Experimental setup

The electrocatalytic degradation experiments were conducted in a column glass cell with a 100 mL capacity where the SACs doped carbon tube and Pt foil acted as cathode and anode, respectively. 20 mg catalyst was mixed with 0.5 mL methanol and five μL Nafion solution and ultrasound for 15 mins. Afterward, the solution was dropped to the FTO glass uniformly and dried in a 60°C oven for further use. The cathode working areas of 6.0 cm^2 . The cathode's applied bias ranges from 0.2 V to 1.2 V (vs. Hg/HgCl_2). The O_2 flow rate varies with a flow rate of 0.1, 0.3, 0.5, and 0.7 L/min, containing $0.1\text{ mol}\cdot\text{L}^{-1}\text{ Na}_2\text{SO}_4$ and 2 ppm IBU. The solution's pH was adjusted to a particular value (i.e., 2.5, 3.5, 5.5, 7.5, 9.5, and 11.5) by 0.01 M H_2SO_4 and NaOH, respectively. A 3 mL suspension was collected from the reaction cell at given time intervals during ORR. The extracted sample was filtered through a $0.22\text{ }\mu\text{m}$ PTFE syringe filter (Acrodisc, Pall Corporation) to remove the residual catalysts. The concentration of PPCPs was measured using a high-performance liquid chromatography (HPLC) system (Waters, USA).

2.4. Determination of hydroxyl radical's amount

The content of $\bullet\text{OH}$ generated during ORR was detected by the photofluorescence (PL) signal of hydroxybenzoic acid (hydroxycoumarin), obtained from the capture of $\bullet\text{OH}$ by benzoic acid, which indicates the concentration of $\bullet\text{OH}$. The details include 100 mL H_2O containing 100 mg benzoic acid (40 mg coumarin); the suspension was adjusted to pH 3.5. Then, at different time intervals, the solution was extracted and measured by PL spectroscopy to calculate the contents of $\bullet\text{OH}$ (excitation wavelength: 300 nm of hydroxybenzoic acid and 332 nm of hydroxycoumarin).

2.5. Determination of H_2O_2 generation amount

The concentration of the generated H_2O_2 was measured by UV-vis spectroscopy according to the color change of the titanium(IV)-peroxide complex. Firstly, 27.2 mL of concentrated H_2SO_4 was mixed with about 30 mL of distilled water. Next, 3.54 g of potassium titanium (IV) oxalate, $\text{K}_2\text{TiO}(\text{C}_2\text{O}_4)_2$ was added and made up to 1 L with distilled water. Then, 5 mL titanium reagent and 5 mL sample were transferred into a 25 mL calibrated flask and made up to 25 mL calibration. Afterward, the absorbance of the solution was measured at 400 nm. A blank one consisting of a 5 mL titanium reagent and a 5 mL sample without H_2O_2 should also be calculated.

The concentration of H_2O_2 is calculated by taking $\epsilon_{400} = 935\text{ L}\cdot\text{mol}^{-1}\cdot\text{cm}^{-1}$ as the molar absorptivity of the titanium(IV)-peroxide complex. For x mL of sample per 25 mL of solution, the concentration of hydrogen peroxide (in moles per liter) is given by:

$$[\text{H}_2\text{O}_2] = \frac{(A - A_b)}{37.4xl}$$

Where A and A_b are the absorbances of the test and blank solutions, respectively, and l is the path length of the spectrophotometer cell in centimeters.

2.6. Characterization

In this study, the concentration of pharmaceuticals and personal care products (PPCPs) was analyzed using a high-performance liquid

chromatography (HPLC) system. The degradation byproducts were identified utilizing an Ab-Sciex QTRAP® 4500 electrospray Ionization-triple quadrupole mass spectrometry (ESI/MS) system in the negative ionization mode. The mineralization rate of PPCPs was determined by employing a TOC analyzer (TOC-VCPH, Shimadzu, Japan), while ICP-OES was utilized to measure the loading and leaching of Mo ions. The crystalline structure of the materials was investigated using an X-ray diffraction spectrometer (XRD, PW-1830, Philips, France). Moreover, the metallic surface sites of the catalysts before and after the reaction were analyzed using X-ray photoelectron spectroscopy (XPS) with an X-ray photoelectron spectrometer (PHI 5600, Physical Electronics Inc., USA). The morphology of the samples was characterized using a scanning electron microscope (SEM, TM3030, Hitachi, Japan) and a transmission electron microscope (TEM, JEM-2010, JEOL, Japan). Raman analysis was conducted using a Renishaw micro-Raman system, and Fourier transform infrared (FTIR) spectroscopy (Thermo Scientific Nicolet iS5, America) was employed to obtain the FTIR spectra. Finally, aberration-corrected high-angle annular darkfield scanning transmission electron microscopy (HAADF-STEM, FEI Themis Z, America) was used to investigate the single atomic morphology of the samples. Raman spectroscopy was utilized to identify and analyze the Raman spectra (Horiba Scientific LabRAM HR Evolution, France). By using these analytical techniques, a comprehensive understanding of the PPCPs and their degradation byproducts, as well as the materials used as catalysts for their removal, was achieved.

2.7. EXAFS analysis

Data reduction, analysis, and EXAFS fitting were performed using the Athena and Artemis software packages [15]. The energy calibration of the sample was conducted through a standard Mo foil, which as a reference was simultaneously measured. First, a linear function was subtracted from the pre-edge region; then, the edge jump was normalized using Athena software. Next, the $\chi(k)$ data were isolated by removing a smooth, three-stage polynomial approximating the absorption background of an isolated atom. Finally, the k^3 -weighted $\chi(k)$ data were Fourier transformed after applying a Hanning window function ($\Delta k = 1.0$). For EXAFS modeling, The global amplitude EXAFS (C_N , R , S_0^2 , σ^2 , and ΔE_0) were obtained by nonlinear fitting, with least-squares refinement, of the EXAFS equation to the Fourier-transformed data in R-space, using Artemis software, EXAFS of the Mo foil is fitted, and the obtained amplitude reduction factor S_0^2 value (0.951) was set in the EXAFS analysis to determine the coordination numbers (CNs) in the Mo-C scattering path in the sample. For Wavelet Transform analysis, the $\chi(k)$ exported from Athena was imported into the Hama Fortran code [16]. The parameters were listed as follows: R range, 1–3.5 Å; k range, 0–13.0 Å⁻¹ for sample (0–13.0 Å⁻¹ for Mo foil, MoO₂, and MoO₃); k weight, 2; and Morlet function with $\kappa = 10$, $\sigma = 1$ was used as the mother wavelet to provide the overall distribution.

2.8. Electrochemical properties test

To investigate the activity of oxygen reduction reaction (ORR), a rotating ring-disk electrode (RRDE) was utilized in this study. Initially, a mixture of MeOH and Nafion solution with volumes of 1.0 mL and 0.2 mL, respectively, was prepared and 5 mg of catalyst powder was added to it. Next, 10 µL of the resulting homogeneous mixture solution underwent ultrasonic treatment for 30 min, after which it was deposited onto a glassy carbon disk electrode with a surface area of 0.283 cm². The prepared working electrode was then dried at room temperature before being subjected to RRDE and rotating disk electrode (RDE) tests using a computer-controlled electrochemical station (Princeton, USA). The three-electrode system included a modified glassy carbon disk working electrode, a reference electrode of KCl-saturated Hg/Hg₂Cl₂, and a

counter electrode of platinum wire, which was submerged in 0.1 mol/L Na₂SO₄ under O₂ at pH = 3.5. By utilizing these methods, the ORR activity of the catalyst was effectively evaluated.

The selectivity of H₂O₂ and the corresponding electron transfer number (n) of ORR can be calculated according to the following equations:

$$H_2O_2\% = 200 \times \frac{I_R/N}{I_D + I_R/N}$$

$$n = \frac{4I_D}{I_D + I_R/N}$$

Where I_R is the ring electrode current, I_D is the disk electrode current, and N is the collection efficiency (0.37).

$$\frac{1}{J} = \frac{1}{J_k} + \frac{1}{B\omega^{0.5}}$$

$$B = 0.62nF(D_{O_2})^{2/3}\nu^{-1/6}C_{O_2}$$

Where J and J_k are the current density and kinetic current density (mA·cm⁻²) of the LSV by RDE, ω the velocity of electrode rotation (rad), and F the Faraday constant (96,485 C·mol⁻¹). D_{O_2} and C_{O_2} are the oxygen diffusion coefficient (1.9×10^{-5} cm²·s⁻¹) and bulk concentration (1.2×10^{-6} mol·cm⁻²), ν the solution's kinematic viscosity (0.01 cm²·s⁻¹).

2.9. Pseudo-first-order kinetic model

The corresponding kinetic calculation of ORR for degradation of 2 ppm IBU (Fig. S8) was conducted. The kinetics were investigated using a pseudo-first-order kinetic model, as shown in the following equation.

$$-\ln(C/C_0) = kt,$$

Where C_0 and C represent organic matter concentration at time $t = 0$ and t , respectively, k (min⁻¹) should be the rate constant.

2.10. DFT calculation methods

All spin-polarized DFT calculations in this work were carried out using the Vienna Ab-initio Simulation Package (VASP) [17]. The projector augmented wave (PAW) method [18], and the Perdew-Burke-Ernzerhof (PBE) [19] functional utilizing the generalized gradient approximation (GGA) [20] were applied throughout the calculations. The kinetic energy cut-off was set as 400 eV, and the structure optimization force threshold was 0.05 eV/Å. For the model construction, we built one nitrogen atom doping of the ten layers of the tube-5_5 slab, and one also built the single Mo atoms, Mo₅, and MoO₃ clusters supported on the N-tube-5_5 outer surface. A corresponding $2 \times 1 \times 1$ k -point mesh was used for all these models, and the slabs were allowed to relax fully. We used a vacuum height of 15 Å to eliminate the interaction between neighboring tubes in the X and Y directions.

The ORR performance was characterized by the reaction-free energy of the adsorbed intermediate (*OOH), defined as:

$$\Delta G = \Delta E + \Delta ZPE - T \times \Delta S$$

Where ΔG , ΔE , ΔZPE and $T \times \Delta S$ are the change of the free energy, total energy from DFT calculations, zero-point energy, and entropic contributions (T was set to be 298.15 K), respectively. The zero-point energy and $T \times \Delta S$ can be obtained from vibrational frequencies derived from Hessians' calculation from analytic gradients on a single molecule in a vacuum or adsorbates. The values used for corrections of ΔZPE and $T \times \Delta S$ were calculated by frequencies and listed in Table S3.

3. Results and discussion

3.1. Properties of single Mo atoms/clusters doped on carbon tube

3.1.1. Composition and morphology

Fig. 1a illustrates the simple methodology of preparing single Mo atoms/clusters doped on carbon tubes. Specific amounts of carbon tubes and ammonium heptamolybdate tetrahydrate were mixed and ground using a ball-milling method for 2 h, followed by calcination under Ar flow. The successful preparation was confirmed by the X-ray diffraction (XRD) results. In Fig. S1a, several characteristic peaks are located at 25.7° , 42.9° , 54.3° , and 78.2° , which are indexed to the (002), (101), (004), and (110) planes of the multi-walled carbon nanotubes [21,22], respectively. After calcination, in addition to the typical peaks of MWCNTs, the characteristic peaks at 34.7° , 38.1° , and 39.6° are allocated to the (100), (002), and (101) planes of Mo_2C (PDF #35-0787) [23], as well as (110), (410), (404) planes for MoO_3 [24], suggesting that apart

from single Mo atoms/clusters existing, Mo_2C and MoO_3 was generated as a by-product. From the Fourier transform infrared (FTIR) spectra (Fig. S1b), the peak at 1234 cm^{-1} arising from aromatic ether AR-O bond disappeared after incorporating Mo atoms/clusters, ascribed to the formation of Mo-C bond that distorted the structure. And the bands around 1259 cm^{-1} , 1647 cm^{-1} , $2900\text{--}3000\text{ cm}^{-1}$, and 3302 cm^{-1} should stem from the C-O stretching, C-C stretching, C-H bending, and -OH stretching [25], respectively. As to Raman spectra (Fig. S1c), the I_D/I_G intensity ratio increased from 1.455 to 1.983, signifying that single Mo atoms/clusters were successfully implanted into the skeleton of the carbon tube [26].

Regarding morphology, the presence of Mo_2C and the uniform dispersion of element Mo in the carbon matrix were confirmed using transmission electron microscopy (TEM) and EDS mapping (Fig. 1b-e and Figs. S2a-b). The uniform atomically dispersed elements Mo, C, N, and O were also identified by SEM (Fig. S3a) and corresponding EDS mapping (Fig. S3b-e). Furthermore, the presence of uniformly dispersed

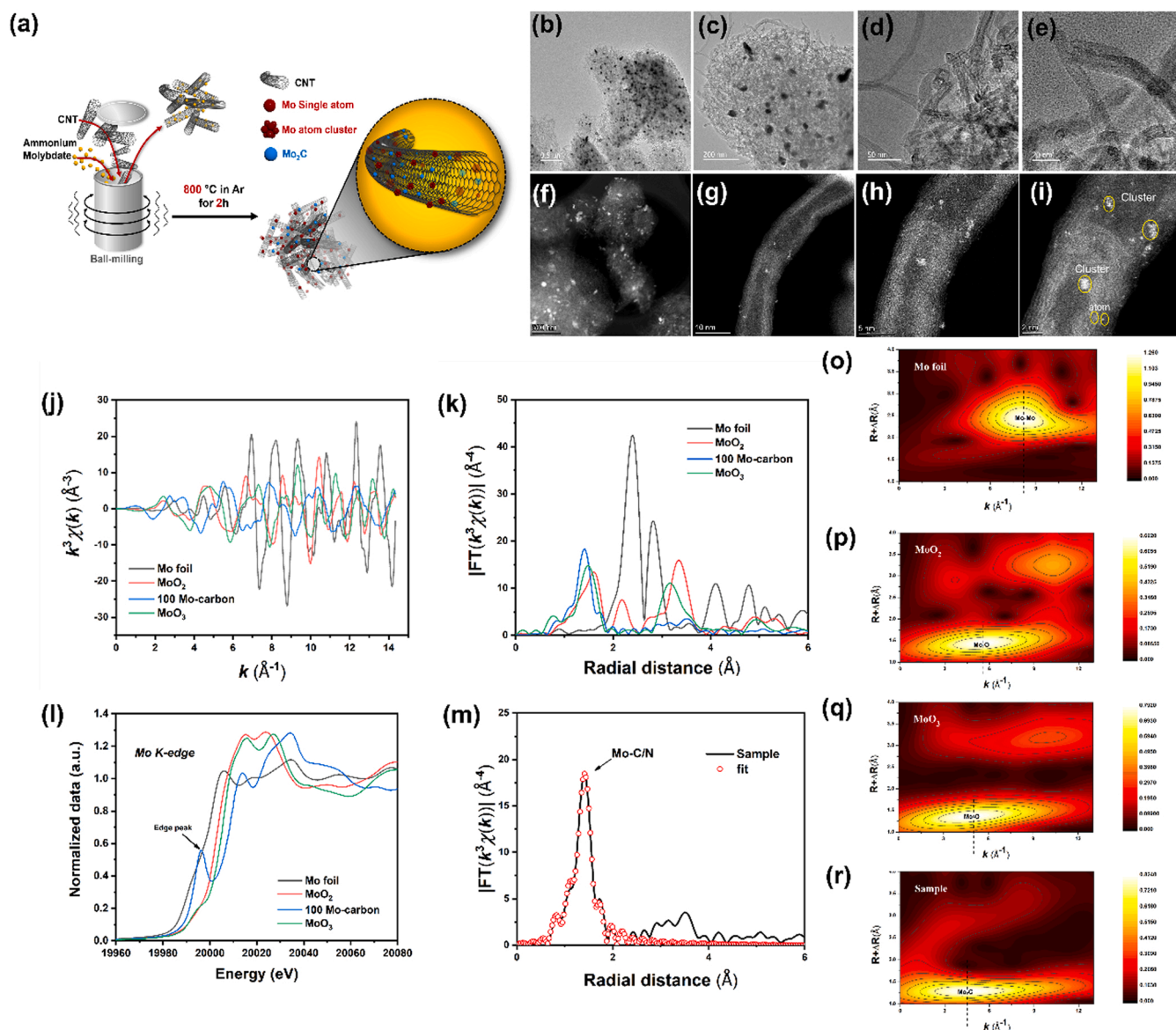


Fig. 1. Material characterization of the single Mo atoms/clusters-based catalyst materials: (a) Preparation methodology of 100 Mo-carbon tube, (b-e) TEM and HRTEM images of the 100 Mo-carbon tube, (f-i) aberration-corrected high-angle annular darkfield scanning transmission electron microscopy (AC HAADF-STEM) images of 100 Mo-carbon tube, (j) k^3 -weighted $\chi(k)$ EXAFS data for Mo foil, MoO_2 , MoO_3 , and 100 Mo-carbon tube, (k) EXAFS spectra of the Mo foil, MoO_2 , MoO_3 , and 100 Mo-carbon tube, (l) XANES spectra of Mo K-edge, (m) Curve fitting of EXAFS (fitting by Mo-C/N), (n-r) Two-dimensional (2D) Wavelet Transform EXAFS plots for $\chi(k)$ EXAFS data collected for Mo foil, MoO_2 , MoO_3 , and 100 Mo-carbon tube.

Mo single atoms/clusters was confirmed using aberration-corrected high-angle annular darkfield scanning transmission electron microscopy (AC HAADF-STEM) (Fig. 1f-i). The HAADF-STEM images revealed the existence of single Mo atoms and clusters, with Mo atoms/clusters randomly implanted into the backbone of the carbon nanotube. On average, the size of a single Mo atom is approximately 0.1 nm. The formation of single Mo clusters, rather than just single Mo atoms, in this case, is mainly due to the high loadings of Mo atoms surpassing its capacity. This leads to single atoms becoming unstable and inclined to stack as clusters [27]. In this case, the specific number of Mo atoms in the clusters cannot be determined merely from the TEM and HAADF-STEM images. Nonetheless, it can be concluded that the bright areas located in the HAADF-STEM images should be clusters rather than nanoparticles due to the fact that, unlike nanoparticles, single atom/clusters do not possess identified lattice fringe.

3.1.2. Surface property

To gain insight into the chemical state of element Mo, both X-ray photoelectron spectroscopy (XPS) and synchrotron-radiation-based X-ray absorption fine structure (XAFS) measurements were employed to confirm the local structure of single Mo atoms/clusters doped on the carbon tube. X-ray photoelectron spectroscopy (XPS) was performed to further verify the impact of different coordination environments on the electronic structure of Mo (Fig. S4). In Fig. S4, the Mo 3d spectra of the 100 Mo-carbon tube are presented. The binding energy of Mo 3d_{5/2} and Mo 3d_{3/2} is 228.9 and 232.8 eV, respectively, which can be indexed to the Mo⁴⁺ state. Moreover, the binding energy at 228.0 and 231.1 eV are attributed to Mo⁰ 3d_{5/2} and Mo⁰ 3d_{3/2}, respectively. Additionally, the peaks observed at 234.5 and 236.1 eV correspond to Mo⁶⁺ 3d_{5/2} and Mo⁶⁺ 3d_{3/2}, respectively. These findings provide valuable insights into the chemical state of element Mo and the local structure of single Mo atoms/clusters doped on the carbon tube. Based on the previous studies [28–30], those peaks all showed a blue or red shift, signifying that the coordination environment of Mo has been changed.

To accurately determine the true states of Mo species in the material, X-ray absorption fine structure (XAFS) characterizations were conducted. Firstly, Mo K-edge XAFS was performed, and Fig. 1j and k show the k^3 -weighted $\chi(k)$ EXAFS data for Mo foil, MoO₂, MoO₃, and 100 Mo-carbon tube. The Fourier-transformed EXAFS curves of the Mo foil, MoO₂, MoO₃, and 100 Mo-carbon tube were also elucidated. In the 100 Mo-carbon tube, the main peak observed was at 1.79 Å, which can be attributed to the Mo-C/N bond. This is distinct from the main characteristic peaks of the Mo-Mo bond in Mo foil, where the peaks were observed at 2.72 Å and 3.14 Å, respectively. These results provide further evidence of the true states of Mo species in the material and contribute to a more comprehensive understanding of the material's properties and characteristics. As the source of element N, its origin was from the precursor of Mo (i.e., (NH₄)₆Mo₇O₂₄·4 H₂O), as evidenced by the full XPS spectra of 100 Mo-carbon tube (Fig. S5a). Meanwhile, the existences of elements O, N, and C are also individually presented (Fig. S5b, c and d). In addition, the peak of MoO₂ and MoO₃ was observed at 2.00 Å and 1.95 Å, respectively. Moreover, the spectra of normalized X-ray absorption near-edge structure (XANES) (Fig. 1l) were obtained for Mo K-edge for Mo foil, MoO₂, MoO₃, and 100 Mo-carbon tube. These spectra demonstrated that the edge positions of 100 Mo-carbon tube were between Mo foil and MoO₂, which suggests that the valence state of Mo in the single Mo atoms/clusters doped on the carbon tube is between 0~+ 4, and closer to + 4. These findings provide additional confirmation of the chemical state of element Mo in the material and contribute to a more comprehensive understanding of the material's properties. This change in the electronic state of Mo may come from the different coordination environments (i.e., Mo-C/N); thus, the use of SACs would provide a promising opportunity to alter the ORR pathway effectively for the EF process. In addition, there is an obvious edge front signal in the sample, indicating that Mo is locally non-centrosymmetric or has poor symmetry due to the coexistence of

Mo₂C and MoO₃ nanoparticles. Furthermore, the least-squares EXAFS fitting for the Fourier-transformed EXAFS curves was performed using a square geometry structure (Fig. 1m). As a result, the model fitted very well with the Mo-C4 coordination. The other relevant results and corresponding parameters are shown in Figs. S6-7 and Table S1. Afterward, a continuous Cauchy wavelet transform analysis of k^3 -weighted EXAFS spectra was carried out to verify the atomic dispersion and geometric configuration of Mo single-atom catalysts (SACs). From Fig. 1(o-r), the wavelet transform plots exhibit intensity maximums at 4.521 Å⁻¹, attributed to the Mo-C bond in the sample. The intensity maximums at 8.231 Å⁻¹ (Figs. 1o), 5.546 Å⁻¹ (Figs. 1p), and 5.027 Å⁻¹ (Fig. 1q) were assigned to the Mo-Mo bonds from Mo foil, Mo-O bond from MoO₂, and MoO₃, respectively, which are absent in the contour plots of the sample. These results convincingly prove the atomic dispersion of Mo species in single Mo atoms/clusters doped on carbon tubes.

3.2. ORR performance of single Mo atoms/clusters doped on carbon tube

3.2.1. Preliminary results and electrochemical property

The ORR performance of single Mo atoms/clusters doped on carbon tube was evaluated in a three-electrode system with calibrated reference electrodes (i.e., Hg/HgCl₂) (Fig. 2a). The impact of Mo precursor (i.e., (NH₄)₆Mo₇O₂₄·4 H₂O) was investigated (Fig. 2b), and it was found that if the Mo precursor was determined to be 100 mg, the tandem ORR and EF process could exhibit the optimal degradation (ca. 98%). This is because too much or too little doping of single Mo atoms/clusters into the carbon matrix can result in a decrease in the current density of the materials. Further, the detailed and specific electrochemical properties were evidenced by linear sweep voltammograms (LSV) (Fig. 2c), onset potential (Fig. 2e), Tafel plots (Fig. 2d), and electrochemical impedance spectroscopy (EIS) (Fig. 2f) of different materials, including carbon tube, 25 Mo-carbon tube, 50 Mo-carbon tube, 75 Mo-carbon tube, 100 Mo-carbon tube, 150 Mo-carbon tube, and 200 Mo-carbon tube, respectively. More specifically, from the LSV curves (Fig. 2c), we can see that the current density of various types of single Mo atoms/clusters doped on the carbon tube was dramatically lifted, compared to that of the carbon tube. This observation suggests that the doping of Mo atoms/clusters into the carbon tube significantly enhances the electrochemical activity of the material. The onset potential of carbon tube, 25 Mo-carbon tube, 50 Mo-carbon tube, 75 Mo-carbon tube, 100 Mo-carbon tube, 150 Mo-carbon tube, and 200 Mo-carbon tube is determined to be -0.89 V, -0.65 V, -0.64 V, -0.87 V, -0.92 V, -0.66 V, and -1.06 V, respectively. The corresponding Tafel slope is 48 mV/dec, 11 mV/dec, 9 mV/dec, 12 mV/dec, 23 mV/dec, 14 mV/dec, 59 mV/dec, respectively. The 50 Mo-carbon tube possessed the lowest onset potential (-0.64 V) and lowest Tafel slope (9 mV/dec). The EIS spectra (Fig. 2f) showcased that the 100 Mo-carbon tube possessed the best charge-transfer property, indicating that the single Mo atoms/clusters successfully tuned the electronic property of the carbon tube. Meanwhile, the Tafel slopes (Fig. 2d), which were derived from LSV curves, revealed that the 100 Mo-carbon tube produced a lower Tafel slope (23 mV/dec) than the carbon tube (48 mV/dec), and the current density of the 100 Mo-carbon tube was calculated to be 2.91 mA/cm². This indicates that the 100 Mo-carbon tube exhibits superior electrocatalytic activity for the ORR compared to the carbon tube. To ensure that O₂ is indeed involved in the ORR, the cyclic voltammetry and corresponding ORR performance (Fig. S8) for the degradation of 2 ppm IBU of 100 Mo-carbon tube under O₂ and N₂ were investigated, respectively. A prominent O₂ reduction peak at -0.32 V (vs. RHE) was observed (Fig. 2g), reflecting its high ORR activity. In retrospect of the IBU degradation rate, the efficiency was greatly hampered by the diffusion of N₂ (merely 20%, Fig. S8), thus highlighting the significant role of O₂ in this case. In addition, the amount of H₂O₂ produced during the ORR was determined by a spectrophotometric method using the titanium (IV)-peroxide complex[31]. The results showed that about 1.06 ~ 4.24 mmol h⁻¹ H₂O₂ was produced in a 0.1-liter H₂O system within 30 mins (Fig. 2h),

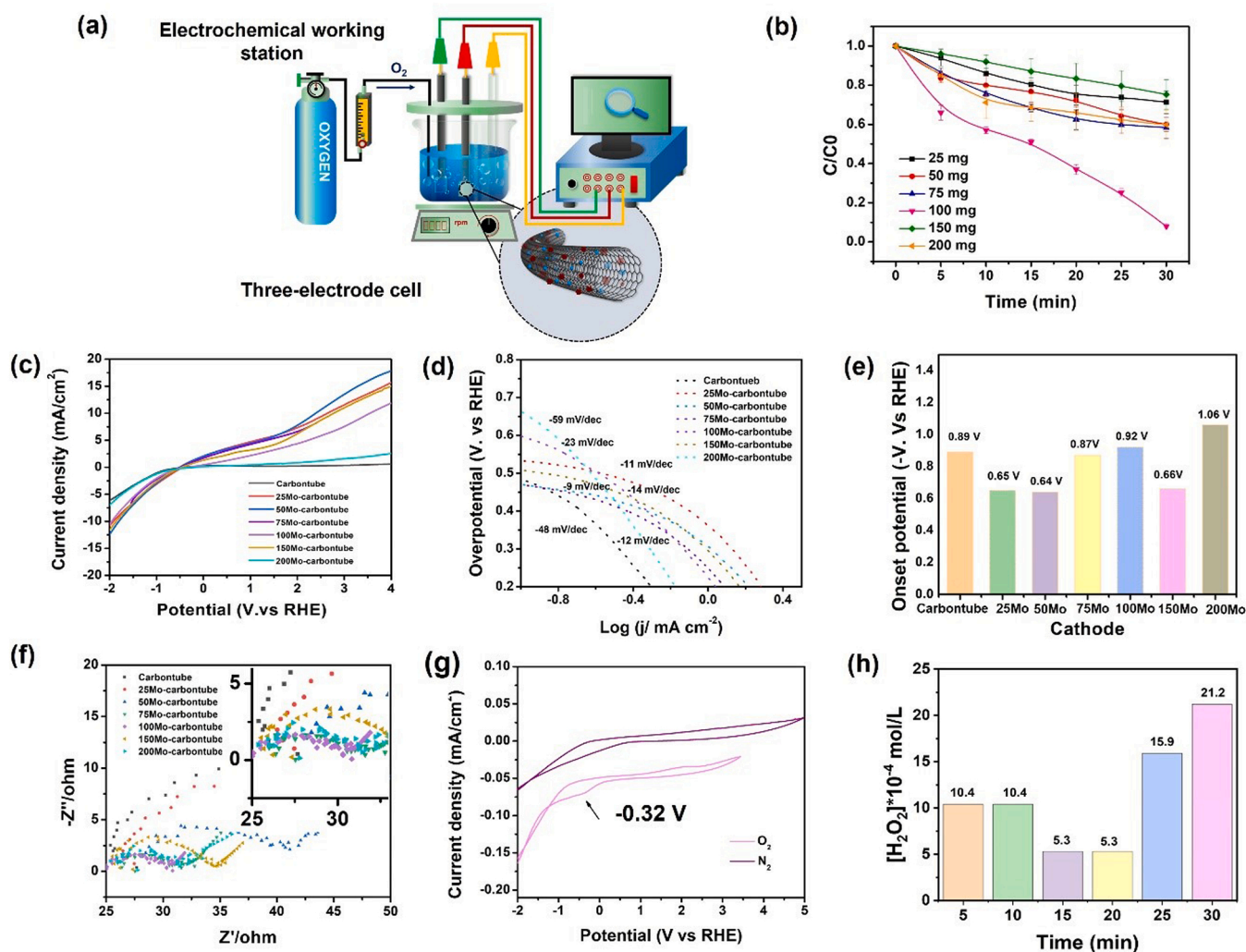


Fig. 2. Characterization of the electrochemical properties of the single Mo atoms/clusters-based catalyst materials: (a) set-up diagram for the ORR test, (b) effect of various Mo precursors, (c) linear sweep voltammograms, (d) Tafel plots, (e) onset potentials of the carbon tube, 25 Mo-carbon tube, 50 Mo-carbon tube, 75 Mo-carbon tube, 100 Mo-carbon tube, 150 Mo-carbon tube, and 200 Mo-carbon tube, (f) EIS plots of the carbon tube, 25 Mo-carbon tube, 50 Mo-carbon tube, 75 Mo-carbon tube, 100 Mo-carbon tube, 150 Mo-carbon tube, and 200 Mo-carbon tube, (Inset pic: enlarged illustration of EIS data), (g) cyclic voltammetry curves under saturated N₂ and O₂ conditions (0.1 M NaSO₄, pH 3.5, 10 mV/s), respectively, and (h) the concentration of the generated H₂O₂ during ORR tests.

surpassing most research reported in recent years and summarized in Table S2.

3.2.2. Effects of various parameters and kinetic calculation

Indeed, it is well known that several factors, such as the pH value, applied cathodic bias, O₂ flow rate, and catalyst dosage, can influence the ORR performance. These factors need to be carefully optimized and controlled in order to achieve the best possible ORR performance in electrochemical systems. [32]. Given this, we have chosen some parameters (e.g., pH value, applied cathodic bias, O₂ flow rate, and catalyst dosage) to investigate their impact deeply. Nonetheless, most ORR was operated in an alkaline environment (pH=10.0) [33,34]. Firstly, we explored the various pH values, ranging from 2.5 to 11.5 (Fig. S9a). The results elaborated that when the pH value was fixed at 5.5, it could achieve the optimal performance (92%) of in-situ generated H₂O₂ in ORR for IBU degradation, with a corresponding kinetic *k* value of 0.03054 min⁻¹ (Fig. S10a). Surprisingly, it is worth noting that the ORR can be effective in both acidic (e.g., pH 3.5) and alkaline conditions (e.g., pH 9.5 and 11.5) with a kinetic constant of 0.01216 min⁻¹ and 0.00949 min⁻¹, respectively. This effectiveness is mainly ascribed to the dissolved O₂ reacting with protons and hydroxide ions, forming H₂O₂ via a 2-electron pathway [35]. As for the applied cathode bias, the results

revealed that -1.0 V (vs. Hg/HgCl₂) was the most suitable value for the cathode (Fig. S9b). It was supposed that if the applied voltage was too low or too high, this would give rise to insufficient external power for O₂ reduction and H₂ production, as well as the reaction of excess H₂O₂ with •OH, ultimately leading to lower degradation efficiency. Then, the O₂ flow rate was also investigated (Fig. S9c). When the O₂ flow rate increased from 0.1 to 0.3 L/min, the IBU degradation efficiency increased from 27% to 88.3%, and the reaction kinetic constant *k* increased from 0.00493 to 0.02368 min⁻¹ (Fig. S10c). This phenomenon was attributed to the enhancement of mass transport of IBU molecules towards the active catalytic sites caused by the convection of O₂ [36]. However, the IBU degradation efficiency significantly decreased when the O₂ flow rate continuously increased to 0.7 L/min, possibly due to the intense oxygen convection, which is difficult for IBU molecules to access the active sites. Lastly, in terms of the catalyst dosage, a similar trend was observed, likely due to the increasing number of IBU molecules moving towards active catalytic sites, similar to the O₂ flow rate effect. The degradation efficiency increased from 38% to 82%, and the constant kinetic *k* increased from 0.00728 min⁻¹ to 0.0105 min⁻¹ (Fig. S10d). However, when the catalyst amount increased to 30 mg, the IBU degradation efficiency was suppressed, mainly arising from too much produced H₂O₂ acting as •OH scavenger. LC-MS analysis was used

to study the specific IBU degradation pathway, with more details shown in Figs. S11 and S12. The degradation efficiency, capacity, and performance of this cathode were compared with other reported materials, as summarized in Table S3. The degradation efficiency, time cost, and generated H_2O_2 amount exhibited remarkable results compared to other materials.

3.3. Mechanism investigation on ORR tandemly removing organic contaminants

3.3.1. Control experiments

The mechanism of ORR for tandemly removing IBU was investigated in detail, as shown in Fig. 3a. Several batch experiments were conducted, including $\text{FTO}+\text{H}_2\text{O}_2$, $\text{Cat}+\text{H}_2\text{O}_2$, $\text{EC}+\text{Cat}+\text{H}_2\text{O}_2$, and $\text{EC}+\text{Cat}+\text{O}_2$ systems. Interestingly, the degradation efficiency of $\text{FTO}+\text{H}_2\text{O}_2$ was found to be better than $\text{Cat}+\text{H}_2\text{O}_2$, which was attributed to the heterogeneous Fenton process rather than the homogenous Fenton process. However, when a voltage was applied to the heterogeneous Fenton process (i.e., $\text{EC}+\text{Cat}+\text{H}_2\text{O}_2$ system), the efficiency was enhanced, highlighting the role of electrons (e^-) in decomposing H_2O_2 in this case. Surprisingly, it was also found that the degradation efficiency of the $\text{EC}+\text{Cat}+\text{O}_2$ system was better than the $\text{EC}+\text{Cat}+\text{H}_2\text{O}_2$ system. This indicates that the tandemly constructed ORR with an in-situ generated H_2O_2 system is superior to the $\text{EC}+\text{Cat}+\text{H}_2\text{O}_2$ system, which saves the synthesis and transportation costs of H_2O_2 in the EF process. These results provide valuable insights into the mechanism of the ORR process and highlight the potential of this approach for efficient

wastewater treatment.

3.3.2. Reactive oxygen species (ROSs) detection and corresponding catalysis mechanism

Further, the ROSs were detected using MeOH, p-BQ, and Trp to scavenge the $\bullet\text{OH}$, $\text{O}_2^{\bullet-}$ and $^1\text{O}_2$. As elucidated in Fig. 3b, the $\bullet\text{OH}$ radicals play a leading role in this case. If sacrificing $\text{O}_2^{\bullet-}$ radicals and singlet oxygen, the degradation efficiency can be significantly improved because $\text{O}_2^{\bullet-}$ radicals are intermediates during ORR, and partial hydroxyl radicals are converted into singlet oxygen. Also, the existence of $^1\text{O}_2$ and $\text{O}_2^{\bullet-}$ was validated by the EPR in Fig. S13. In Fig. 3c, the intensity of $\bullet\text{OH}$ in the $\text{E} + \text{Cat} + \text{O}_2$ is higher than $\text{E} + \text{Cat} + \text{N}_2 + \text{H}_2\text{O}_2$, explaining why the degradation efficiency of $\text{E} + \text{Cat} + \text{O}_2$ is better than $\text{EC} + \text{Cat} + \text{H}_2\text{O}_2$ (Fig. 3a). Also, it confirmed that the generated H_2O_2 stems from O_2 instead of H_2O . Additionally, we can conclude from the single H_2O_2 system that the metallic Mo ions could collaboratively decompose H_2O_2 . This proportion belongs to the heterogeneous Fenton reaction.

To thoroughly investigate the catalytic reactions occurring on the catalyst surface and in the aqueous solution, benzoic acid and coumarin were employed as probe molecules to measure the concentration of hydroxyl radicals ($\bullet\text{OH}$) on the catalyst surface and in the solution, respectively. Owing to its high solubility in water, the carboxyl group of benzoic acid readily complexes with metal ions on the catalyst surface. Consequently, benzoic acid is capable of determining the total concentration of $\bullet\text{OH}$ (both on the catalyst surface and in the solution) within the system. The results depicted in Fig. 3d demonstrate a substantial increase in the concentration of $\bullet\text{OH}$. However, the concentration of

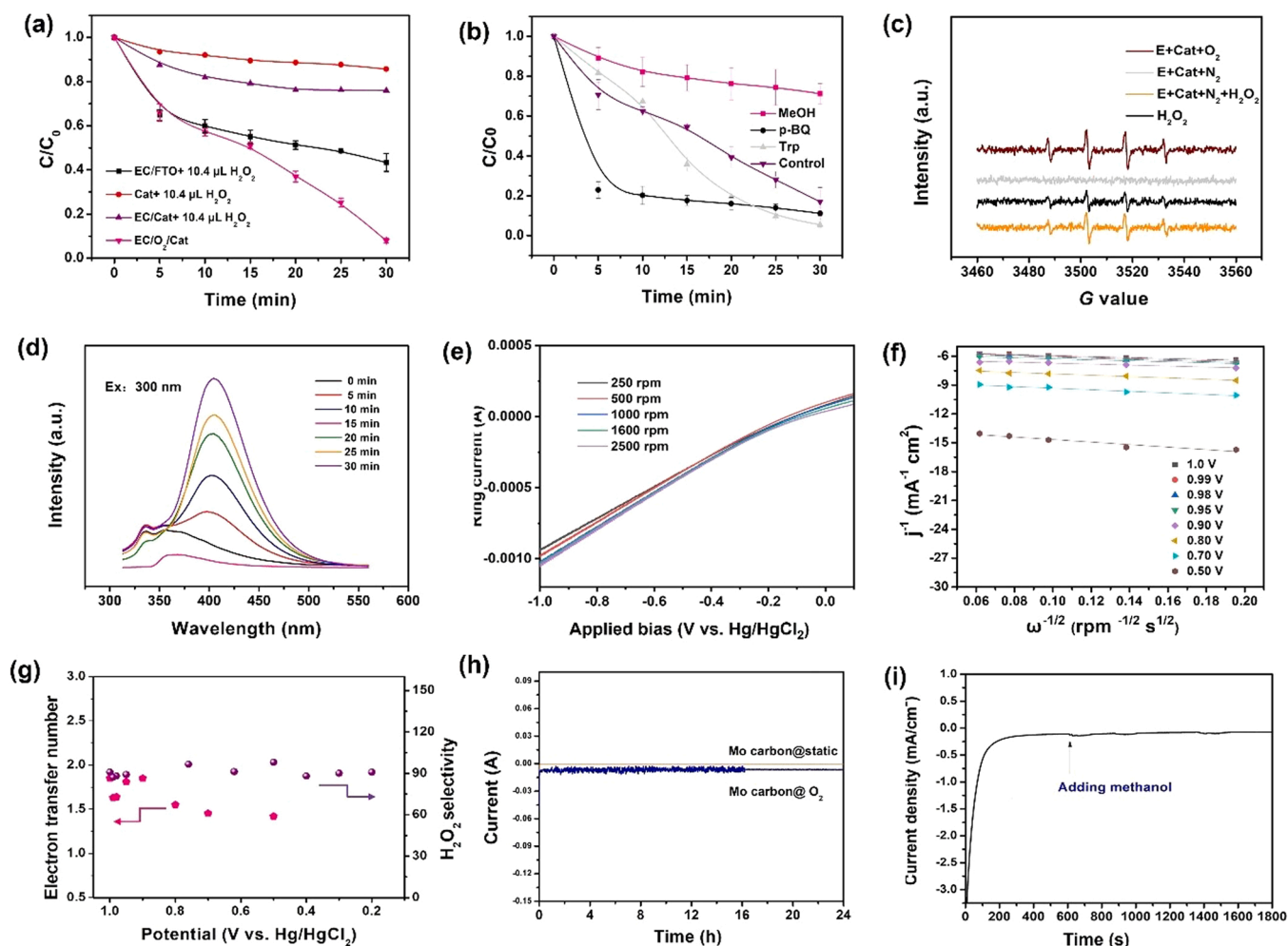


Fig. 3. Mechanism investigation of single Mo atoms/clusters doped on carbon nanotube in ORR: (a).

•OH in the solution, as indicated by the coumarin probe, significantly decreased with time (Fig. S14). At 15 min, the degradation process should have depleted most of •OH radicals in the solution, leading to the lowest intensity. This is well consistent with the lowest production of H₂O₂ shown in Fig. 2 h (5.3×10^{-4} mmol/L).

3.3.3. Electron transferring mechanism

Fig. 3e presents the voltammograms for single Mo atoms/clusters doped on carbon tubes, which increase with the rotating addition rate. The electron transfer number (*n*) during the ORR is calculated to be approximately 2.0 from the Koutecky-Levich (K-L) plots (Fig. 3f), with a potential range of 0.8–1.6 V vs. SCE. The static state and O₂ purging demonstrate the stability of the cathode, respectively, as the current exhibits negligible fluctuation even after 24 h. In the LSV curves (Fig. S15), the current density decreases only slightly after 10000 CV cycles, indicating its convincing stability. The electrocatalytic reduction of H₂O₂ is also verified by linear sweep voltammetry (LSV) (Fig. S16). The reduction of H₂O₂ occurs due to the decreasing current density after H₂O₂ addition, referring to the 2-electron oxygen reductive H₂O₂ intermediate simultaneously stepped by 1-electron electrocatalytic reduction toward •OH. We also confirmed that the applied bias could directly reduce H₂O₂, as shown in Fig. S17. Under this condition, we directly added commercial H₂O₂ into the system instead of ORR. We observed that the IBU degradation efficiency improved with the increasing addition of H₂O₂, compared to that without extra electrocatalysis. Furthermore, the catalyst exhibited no oxidation effect when acting as an anode. The leaching of Mo ions at various time intervals was also detected; the concentration of Mo increased from 0.03971 ppm to 0.04609 ppm (Fig. S18), accounting for 0.0023045%wt. of the catalyst. Importantly, the Mo leaching is less than 70 mg L⁻¹, which is even below the "Guidelines for Drinking-Water Quality, 4th edition" (World Health Organization). Such a low leaching rate for molybdenum enables the Mo-based catalyst to be potentially viable for actual wastewater treatment applications.

3.3.4. Reactor design

The reactor design is crucial for the efficiency of the ORR process, especially if it is to be applied to industrial applications. Therefore, three other types of reactors (separating the anode and cathode into two different cells) were selected, including a salt bridge incorporated cell, a sand core H-type reaction cell, and a proton exchange membrane (PEM) H-type reaction cell, as illustrated in Fig. S19a and Figs. S20a and b, respectively. The IBU degradation efficiency was significantly reduced to 29%, 51%, and 48%, respectively, which was attributed to the insufficient generation of H₂O₂ when the anode and cathode were separated. Additionally, the IBU degradation efficiency for the integrated system (without O₂ purging) was investigated, and the efficiency (Fig. S21) was suppressed to approximately 37%. Correspondingly, the correlated generated H₂O₂ yield was approximately $8.913\text{--}35.652 \times 10^{-4}$ mol/L (within 30 mins, Fig. S22), indicating that H₂O₂ is still generated without external O₂. Preliminary results suggest that this portion of H₂O₂ is produced by the oxidation of water molecules on the anode (Pt). As mentioned above, about 1.06–4.24 mmol h⁻¹ H₂O₂ was produced in a 0.1-liter H₂O system within 30 mins (Fig. 2 h) in an integrated approach, which is on average lower than that of the integrated one without O₂, due to the continuous decomposition of H₂O₂ during the process. These results emphasize the importance of reactor design in achieving efficient ORR processes for practical applications. Furthermore, we summarized the H₂O₂ yield of three systems in the cathode (Fig. S23), including the integrated system in a cell without O₂, the H-type reaction cell with O₂, and the integrated system in a cell with O₂, the yield without O₂ system is higher than that of the with O₂ system, owing to the insufficient H₂O₂ decomposition in this case, well indexed to the degradation efficiency. In the H-type cell (PEM), its H₂O₂ yield is lower than the two integrated systems, even below the detection limit at several intervals. The external O₂ plays a vital role in ORR, and the

section of O₂ where the anode is generated devoted a lot to the H₂O₂ yield in the cathode, and the integrated system in a unit cell is crucial to the degradation efficiency.

the efficiency of Fenton process by the 100 Mo-carbon tube with the electrochemically generated H₂O₂ and directly dosed H₂O₂ (experimental condition: 0.1 L solution, applied voltage: -1.0 V, flow rate = 0.1 L/min, and [electrolyte] = 0.1 mol/L), (b) scavenger test for the degradation efficiency of 2 ppm IBU (methanol: •OH; isopropanol: •OH; p-BQ: O₂^{•-}; Trp: ¹O₂), (c) EPR spectra for the detection of •OH in the presence of 5,5-dimethyl-1-pyrrolidine-oxide (DMPO) at room temperature (experimental conditions: 0.1 L solution, applied voltage: -1.0 V, flow rate = 0.5 L/min, and [electrolyte] = 0.1 mol/L), including the E + Cat+O₂ system, E + Cat+N₂ system, H₂O₂ system, and E + Cat+N₂+H₂O₂ system, (d) benzoic acid fluorescence spectrophotometry for detecting •OH at different time intervals, (e) LSV curves of 100 Mo-carbon tube on RRDE in the oxygen-saturated electrolyte at different rotating speeds, potential scan rate: 10 mV·s⁻¹, (f) Koutecky-Levich plots as derived from the LSV curves in (e), (g) electron transfer numbers and H₂O₂ selectivity of cathode on RRDE at different cathodic potentials, (h) i-t curves of 100 Mo-carbon tube at the static state and O₂ purging condition for 24 h at -1.0 V, (i) methanol tolerant sensitivity of the catalyst.

3.3.5. Surface valence changes

Ultimately, fully investigating the mechanism of ORR tandem EF process, the change of the surface metallic valence state of Mo before and after the reaction was evaluated by X-ray photoelectron spectroscopy (Fig. S24). After reaction, two distinct peaks at 228.9 eV and 232.8 eV, representing Mo(IV) 3d_{5/2} and Mo(IV) 3d_{3/2}, disappeared (Fig. S24c), transferring to the location at 233.7 eV and 235.8 eV, referring to Mo(VI) 3d_{5/2} and Mo(VI) 3d_{3/2}, respectively. The two spin-orbit doublets, coinciding with the peaks of Mo(0) 3d_{5/2} and Mo(0) 3d_{3/2} states, are located at 228.0 eV and 231.1 eV, respectively. After reaction, two peaks located at 228.4 eV and 231.4 eV, representing Mo(0) 3d_{5/2} and Mo(0) 3d_{3/2}. This shift is primarily due to the loss of electrons (oxidation effect), thus forming a higher valence state. The Raman spectra also evidence this before and after the reaction (Fig. S25). In the Raman spectra, the primary cause for the red or blue shift of the Raman peaks is the transformation of chemical bonds or the migration of electron clouds, which is induced by changes in bond force and atomic distance[37]. As depicted in Fig. S25, the three peaks of the catalyst are blue-shifted by 9.4, 18.8, and 18.6 cm⁻¹, respectively. This shift can be attributed to the electron clouds on the surface of the 100 Mo-carbon tube transferring to the H₂O₂ molecules, resulting in a shorter Mo-C bond length and a reduced likelihood of collisions between phonons and photons. Consequently, the average collision-free path increases, and the energy loss caused by such collisions decreases. Therefore, the energy of photons scattered by the 100 Mo-carbon tube following the reaction is higher than before, leading to a displacement of the three peaks in the Raman spectra arising from metallic Mo oxidation. Regarding the C 1 s spectra, two noticeable peaks appear after the reaction, which are indexed to -C=O and -COO groups, primarily due to the oxidation of H₂O₂.

3.3.6. Proposed mechanism

Based on the above data analysis, we propose a possible mechanism for the ORR process, as shown in Eqs. 3–12 and Fig. 4. On the anode, O₂ is produced via water oxidation (Eq. 3), which is then adsorbed onto the catalyst surface, leading to the in-situ generation of H₂O₂ (Eq. 4). Additionally, external purging O₂ is also adsorbed onto the catalyst surface to generate H₂O₂ via Eq. 3. The interface Mo^{x+} ions further decompose H₂O₂ into •OH radicals (Eq. 5). Moreover, the applied bias also decomposes H₂O₂ into •OH radicals (Eq. 6). In this case, electro-Fenton plays a major role in the removal of IBU, while the heterogeneous Fenton reaction contributes only a small part. The •OH radicals react with H₂O₂ to produce HO₂[•], which then dissociates into O₂^{•-} (Eq. 7).

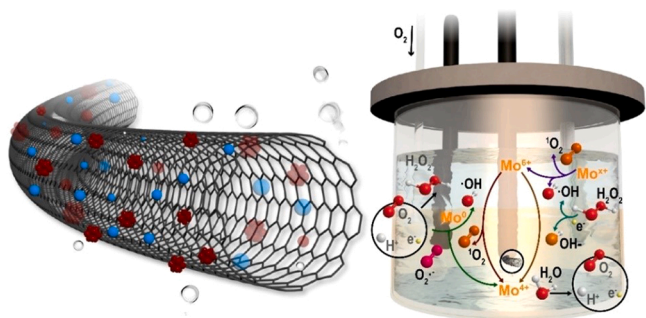
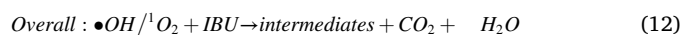
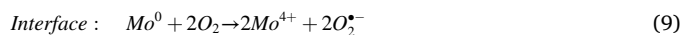
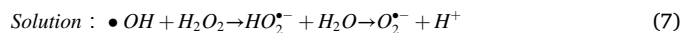
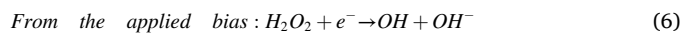
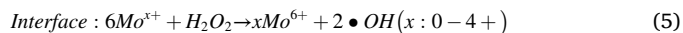
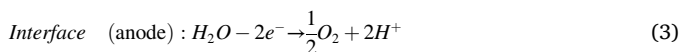


Fig. 4. Brief illustration of a mechanism for single Mo atoms/clusters doped on carbon nanotube in EF process for removing IBU.

Simultaneously, the inter-surface metallic Mo^{6+} is reduced back to Mo^{4+} (Eq. 8), and the interface Mo^0 reacts with O_2 to produce $\text{O}_2^{\bullet-}$ (Eq. 9), which is then reduced back to Mo^{4+} and $^1\text{O}_2$ by the dissolved Mo^{6+} (major way). Interestingly, if $\text{O}_2^{\bullet-}$ is quenched by p-BQ, the intensity of $^1\text{O}_2$ increases (Fig. S26), indicating that Eq. 11 plays a dominant role in forming $^1\text{O}_2$. The $\bullet\text{OH}$ radicals directly convert into $^1\text{O}_2$, rather than the participation of $\text{O}_2^{\bullet-}$ (Eqs. 7–10). Overall, IBU is attacked by ROS and further decomposed into small molecular intermediates, CO_2 , and H_2O (Eq. 12). Thus, the role of electricity in this case is to sequentially synthesize H_2O_2 in the EF process, provide electrons for H_2O_2 decomposition, and benefit Mo^{6+} being reduced to Mo^{4+} .



3.4. DFT calculation

To investigate the electrocatalytic mechanism of O_2 reduction, DFT calculations based on carbon tubes with single Mo atoms/clusters, Mo_2C and Mo oxides were performed, respectively (Fig. 5). Generally, the 2-electron ORR proceeds via a 1-electron oxygen reduction to $\bullet\text{OOH}$ [Eq. (13)] followed by the subsequent 1-electron reduction of $\bullet\text{OOH}$ to H_2O_2 [Eq. (14)]. Therefore, the adsorption binding energy of $\bullet\text{OOH}$ is a crucial descriptor for controlling and modulating the electrocatalytic activity in the 2-electron ORR process.

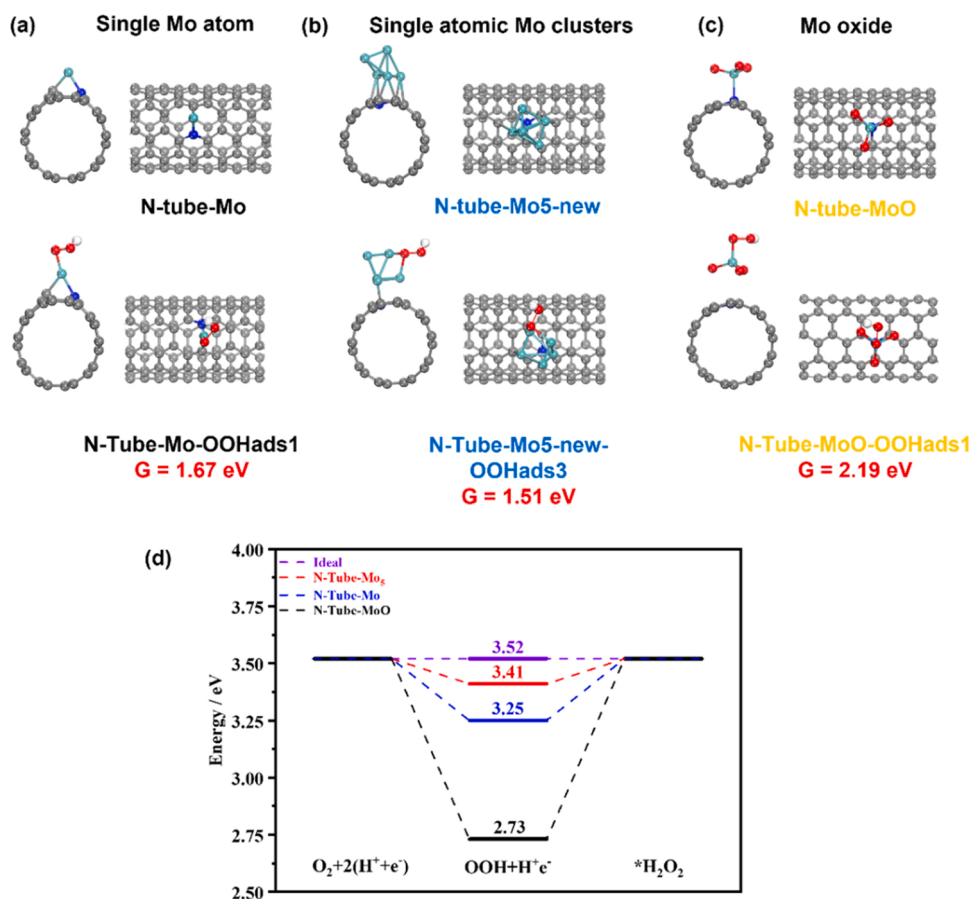


Fig. 5. DFT calculation based on the single Mo atoms/clusters-based catalyst materials: three optimal configurations for (a) single Mo atom doped on carbon tube, Mo_2C doped carbon tube, (b) single Mo clusters doped on carbon tube, and (c) Mo oxide doped on carbon tube, and corresponding Gibbs free energy of $\bullet\text{OOH}$ adsorption, respectively. (d) Free energy diagram for O_2 reduction to H_2O_2 .



Four proposed configurations for single Mo atom doped carbon tube, Mo₂C doped carbon tube, Mo oxide doped carbon tube, single Mo clusters doped carbon tube, and new configuration for single Mo clusters doped carbon tube were displayed in Fig. S27, respectively. Subsequently, the models of single Mo atom, Mo₂C, single Mo clusters, Mo oxide, and new configuration for single Mo clusters doped carbon tube for adsorption of *OOH were presented in Fig. S28, and the

corresponding Gibbs free energy was calculated as well. The results revealed that the lowest Gibbs free energy for single Mo atoms, Mo₂C, single Mo clusters, and Mo oxide for adsorption of *OOH was 1.67 eV, 1.67 eV, 1.51 eV, and 2.19 eV, respectively, indicating that single Mo clusters preferentially act as active sites for *OOH adsorption.; this phenomenon is in line with the work done by Dong et al. [38]. They pointed out that for certain catalytic reactions, the construction of fully exposed metal clusters could help to maximize the reactivity and the atomic efficiency of noble metals, and the activity for single atoms was almost inactive. Also, the activity for Mo₂C and MoO₃ was excluded by implementing experiment (Fig. S29). Worth noting, that both stronger

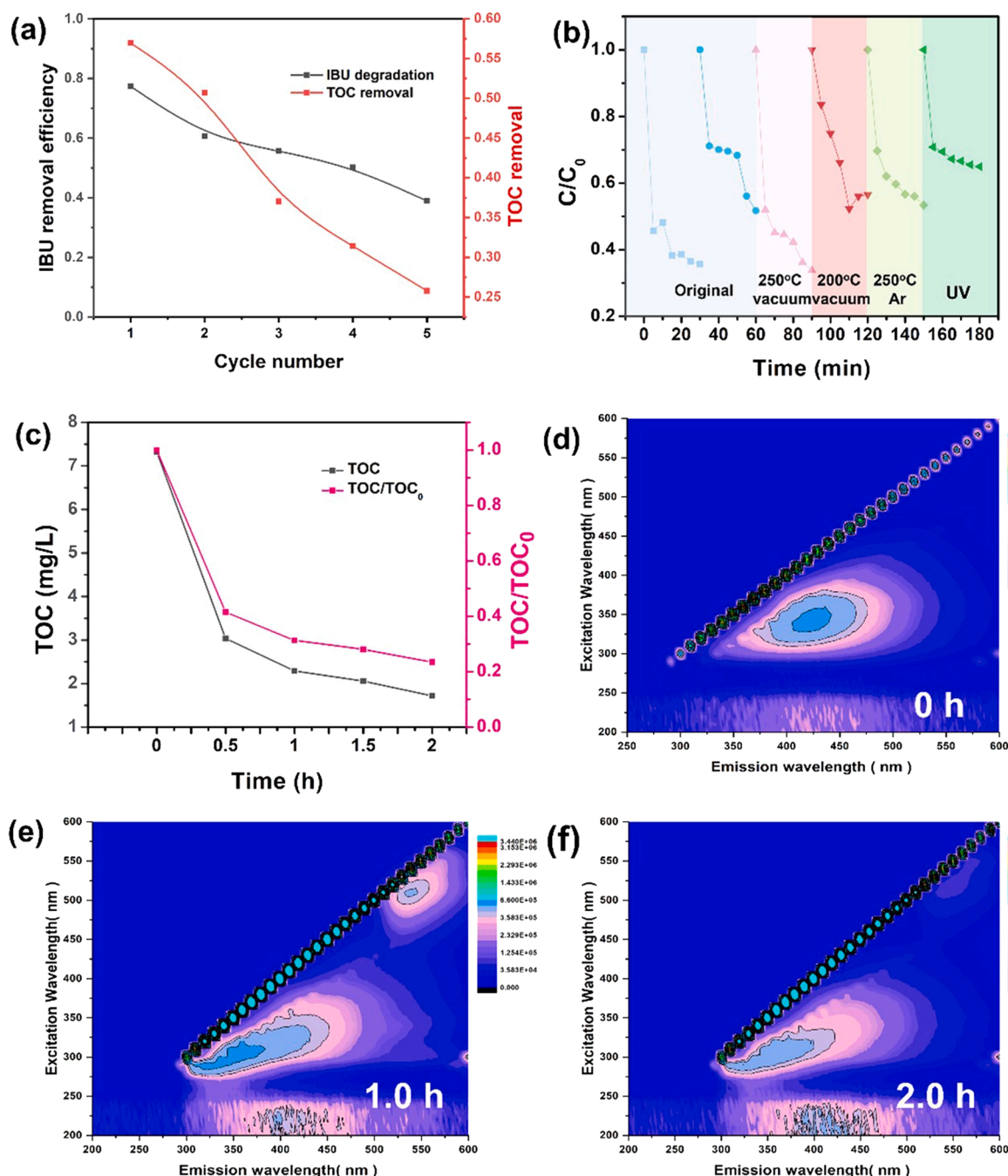


Fig. 6. Recyclability and potential in actual sewage treatment: (a) IBU degradation efficiency and corresponding TOC removal efficiency 5 times, (b) several strategies for lifting the performance of reusability, including vacuum activation at 200 °C and 250 °C, respectively, and 250 °C Ar calcination, as well as UV light irradiation, (c) the TOC removal rate of the sewage for Stanley WTPs. Fluorescence EEM spectra of the sewage from Stanley WTPs treated by ORR at 0 h (d), 1 h (e), and 2 h (f), respectively. The peaks of (d-f) correspond to the Humic acid-like substances (excitation/emission of 250–400/300–550 nm) and the Fulvic-acid-like substances (excitation/emission of 200–250/300–500 nm).

and weaker binding to $^*\text{OOH}$ would bring additional overpotential, causing a bottleneck for the reduction of $^*\text{OOH}$ to H_2O_2 [39]. Notably, for the N-tube with Mo_5 clusters, it was only 0.11 eV downhill to form $^*\text{OOH}$, suggesting that the lowest thermodynamic overpotential of 0.11 eV was required to drive the reaction. However, catalysts such as single Mo atoms, Mo_2C , and MoO_3 with higher thermodynamic overpotentials of 0.27, 0.27, and 0.79 eV were not sufficiently active to promote the 2-electron ORR. Thus, it can be concluded that single Mo clusters would more preferentially favor both the activation of O_2 and desorption of $^*\text{OOH}$. In fact, after loading single Mo clusters, the ORR pathway was altered, as elucidated by the DFT calculation based on the length of O-O bond ($l_{\text{O-O}}$) shown in Figs. S30 and S31.

3.5. Recyclability and potential in actual sewage treatment

In actual sewage treatment, the stability of the catalyst is an essential indicator for measuring its potential in industrial usage. Therefore, we primarily investigated its performance for 5 cycles. The TEM images and XRD patterns demonstrated the material's convincing stability (Fig. S32). In addition, STEM images of the material after reaction still retained the stable morphology of single Mo atoms/clusters (Fig. S33). Moreover, the EDS-mapping images of 100 Mo-carbon also proved its stability (Figure 34). However, the IBU degradation efficiency decreased from 78.4% to 41.2%, accompanied by the TOC removal efficiency ranging from 57.2% to 27.3% (Fig. 6a), which displayed an adverse outcome in practical application. To address this, several strategies were adopted in sequence: the fresh sample was used twice, followed by vacuum treatment at 250 °C and 200 °C, respectively. Then, the sample was treated with argon calcination and UV light irradiation. The outcomes of these several methods unraveled that the facile vacuum treatment at 250 °C is the ideal method (Fig. 6b), providing us with new insights to achieve the goal of reusability for catalysts in actual environmental remediation. Further, the ORR tandemly EF process was adopted to degrade actual wastewater before disinfection from Stanley WTPs in Hong Kong to evaluate its potential usage in existing sewage treatment. After ORR treatment for 30 mins, the TOC removal efficiency achieved a 58% mineralization rate (Fig. 6c), implying its potential in treating actual wastewater. To analyze the changes of natural organic matter (NOM) in the sewage, we used the excitation-emission matrix (EEM) fluorescence spectroscopy to characterize, as illustrated in Fig. 6 (d-f) and Fig. S35. Two types of NOM (i.e., humic-like and fulvic-like substances) were detected in the sewage by referring to the excitation and emission wavelengths. The peaks of Fig. 6d-f correspond to the Humic acid-like substances (excitation/emission of 250–400/300–550 nm) and the Fulvic-acid-like substances (excitation/emission of 200–250/300–500 nm)[40]. After reacting for 30 mins, these two substances were reduced. Subsequently, the decreasing trend of Humic-like and Fulvic-like substances weakened with time prolonging, consistent with the TOC results in Fig. 6c. To expand the scope of transition-metal-based SACs in the ORR tandemly EF process, we synthesized other transition-metal-based SACs doped carbon tubes (i.e., Fe-CNT, Co-CNT, and Ni-CNT). The TEM images (Figs. S35 a-c) and XRD patterns (Figs. S35 d) revealed no apparent aggregation of particles for Fe-CNT, but some particles existed for Co-CNT and Ni-CNT. As for the ORR performance for removing IBU, the results disclosed that Ni-CNT and Fe-CNT possessed an appealing potential in sequential electrocatalysis for tandemly removing organic contaminants.

4. Conclusions

In summary, a novel, solvent-free, zero-waste, and low-cost method was used to prepare single Mo atoms/clusters doped on carbon nanotubes as the cathode material for the EF process. The resulting catalysts were found to be effective in in-situ IBU degradation in both acidic and alkaline conditions. In addition to the applied bias decomposing H_2O_2 into hydroxyl radicals (major route, i.e., EF process), the surface metallic

single Mo atom/clusters also participated in the EF process (minor route, i.e., heterogeneous Fenton reaction). the Mo-based single-atomic materials could impede the 4-electron process, leading to a 2-electron pathway. Accordingly, the integrated three-electrode system in a unit cell achieved a superior degradation efficiency with the essential contribution of O_2 generated on the Pt anode. Furthermore, DFT calculations showed that the single Mo clusters acted as active sites for $^*\text{OOH}$ adsorption and required the lowest thermodynamic overpotential of 0.11 V to drive the reaction. Notably, the tandemly constructed ORR system with in-situ generated H_2O_2 was found to be superior to the EC+Cat+ H_2O_2 system. Moreover, the established EF system was effective in treating the actual sewage effluent. Other transition metals, such as Ni-CNT and Fe-CNT, also exhibited the potential capability for removing IBU, demonstrating the universality of the catalyst structure for AOP application. Equally importantly, the low leaching of Mo ions (0.04609 ppm) suggests that the Mo-based catalyst is suitable for actual wastewater treatment. Overall, this research work provides new directions for the future development of AOPs.

CRediT authorship contribution statement

Chencheng Dong: Validation, Data curation, Resources, Investigation, Formal analysis, Writing-original draft. **Zhi-Qiang Wang:** DFT calculation. **Chao Yang:** Validation. **Xiaomeng Hu:** Validation. **Pei Wang:** Validation. **Xue-Qing Gong:** DFT calculation. **Lin Lin:** Supervision. **Xiao-yan Li:** Conceptualization, Writing - review & editing, Supervision.

Declaration of Competing Interest

The authors declare no competing financial interest.

Data Availability

Data will be made available on request.

Acknowledgment

This research was financially supported by the National Natural Science Foundation of China (Projects 51978369 and 51908316), Chunhui Program from Ministry of Education of China (Project HZKY20220046), Guangdong Basic and Applied Basic Research Foundation (Project 2020A1515111205), and the Research Grants Council (Projects 17210219 and T21 -711/16 R) and the Innovation and Technology Fund (Project ITS/242/20FP) of the Hong Kong SAR Government, China.

Author contributions

The manuscript was written through the contributions of all authors. All authors have given approval for the final version of the manuscript.

Appendix A. Supporting information

Supplementary data associated with this article can be found in the online version at doi:10.1016/j.apcatb.2023.123060.

References

- [1] C. Dong, Z. Wang, Z. Ye, J. He, Z. Zheng, X. Gong, J. Zhang, I.M.C. Lo, Appl. Catal. B-Environ. 296 (2021), 120223.
- [2] C. Dong, M. Xing, J. Zhang, Front. Environ. Chem. 1 (2020).
- [3] F. Xiao, Z. Wang, J. Fan, T. Majima, H. Zhao, G. Zhao, Angew. Chem. Int. Ed. 60 (2021) 10375–10383.
- [4] M. Xing, W. Xu, C. Dong, Y. Bai, J. Zeng, Y. Zhou, J. Zhang, Y. Yin, Chem 4 (2018) 1359–1372.
- [5] M. Melchionna, P. Fornasiero, M. Prato, Adv. Mater. 31 (2019), 1802920.

- [6] M. He, S. Song, P. Wang, Z. Fang, W. Wang, X. Yuan, X. Yuan, C. Li, H. Li, W. Song, D. Luo, Z. Li, Carbon 196 (2022) 483–492.
- [7] A. Wang, J. Li, T. Zhang, Nat. Rev. Chem. 2 (2018) 65–81.
- [8] J. Sun, S.E. Lowe, L. Zhang, Y. Wang, K. Pang, Y. Wang, Y. Zhong, P. Liu, K. Zhao, Z. Tang, Angew. Chem. Int. Ed. 57 (2018) 16511–16515.
- [9] C. Wan, X. Duan, Y. Huang, Adv. Energ. Mater. 10 (2020), 1903815.
- [10] D. San Roman, D. Krishnamurthy, R. Garg, H. Hafiz, M. Lamparski, N.T. Nuhfer, V. Meunier, V. Viswanathan, T. Cohen-Karni, ACS Catal. 10 (2020) 1993–2008.
- [11] K. Jiang, S. Back, A.J. Akey, C. Xia, Y.F. Hu, W.T. Liang, D. Schaak, E. Stavitski, J. K. Nørskov, S. Siahrostami, H.T. Wang, Nat. Commun. 10 (2019) 3997.
- [12] C. Dong, Z. Wang, Z. Ye, J. He, Z. Zheng, X. Gong, J. Zhang, I.M.C. Lo, Appl. Catal. B- Environ. 296 (2021), 120223.
- [13] J. Liu, C. Dong, Y. Deng, J. Ji, S. Bao, C. Chen, B. Shen, J. Zhang, M. Xing, Water Res. 145 (2018) 312–320.
- [14] B. Shen, C. Dong, J. Ji, M. Xing, J. Zhang, Chin. Chem. Lett. 30 (2019) 2205–2210.
- [15] B. Ravel, M. Newville, J. Synchrotron Radiat. 12 (2005) 537–541.
- [16] H. Funke, A. Scheinost, M. Phys. Rev. B 71 (2005), 094110.
- [17] G. Kresse, J. Furthmüller, Phys. Rev. B 54 (1996) 11169–11186.
- [18] P.E. Blöchl, Phys. Rev. B. 50 (1994) 17953–17979.
- [19] J.P. Perdew, K. Burke, M. Ernzerhof, Phys. Rev. Lett. 77 (1996) 3865–3868.
- [20] M.P. Teter, M.C. Payne, D.C. Allan, Phys. Rev. B 40 (1989) 12255–12263.
- [21] X.H. Xia, Z.J. Jia, Y. Yu, Y. Liang, Z. Wang, L.L. Ma, Carbon 45 (2007) 717–721.
- [22] T.A. Saleh, Chem. Eng. J. 404 (2021), 126987.
- [23] J. Liu, P. Wang, J. Fan, H. Yu, J. Yu, ACS Sustain. Chem. Eng. 9 (2021) 3828–3837.
- [24] J. Song, X. Ni, L. Gao, H. Zheng, Mater. Chem. Phys. 102 (2007) 245–248.
- [25] M. Varga, T. Izak, V. Vretenar, H. Kozak, J. Holovsky, A. Artemenko, M. Hulman, V. Skakalova, D.S. Lee, A. Kromka, Carbon 111 (2017) 54–61.
- [26] M. Zhou, Y. Zhao, N. Liao, L. Ren, L. Lyu, G. Quan, M. Gupta, Adv. Eng. Mater. 23 (2021), 2001089.
- [27] C. Dong, M. Marinova, K.B. Tayeb, O.V. Safonova, Y. Zhou, D. Hu, S. Chernyak, M. Corda, J. Zaffran, A.Y. Khodakov, V.V. Ordonsky, J. Am. Chem. Soc. 145 (2023) 1185–1193.
- [28] S. Geng, F. Tian, M. Li, Y. Liu, J. Sheng, W. Yang, Y. Yu, Y. Hou, Nano Res. (2021) 1–8.
- [29] Q. Yan, C. Lian, K. Huang, L. Liang, H. Yu, P. Yin, J. Zhang, M. Xing, Angew. Chem. Int. Ed. 30 (2021) 17155–17163.
- [30] L. Zhang, J. Liang, Y. Wang, T. Mou, Y. Lin, L. Yue, T. Li, Q. Liu, Y. Luo, N. Li, Angew. Chem. Int. Ed. 133 (2021) 25467–25472.
- [31] R.M. Sellers, Analyst 105 (1980) 950–954.
- [32] G. Zhang, L. Zhao, X. Hu, X. Zhu, F. Yang, Appl. Catal. B-Environ. 313 (2022), 121453.
- [33] S. Cai, Z. Meng, H. Tang, Y. Wang, P. Tsiakaras, Appl. Catal. B-Environ. 217 (2017) 477–484.
- [34] P. Strasser, Account. Chem. Res. 49 (2016) 2658–2668.
- [35] F. Liu, Y. Liu, Q. Yao, Y. Wang, X. Fang, C. Shen, F. Li, M. Huang, Z. Wang, W. Sand, J. Xie, Environ. Sci. Technol. 54 (2020) 5913–5921.
- [36] Y. Liu, F. Liu, Z. Qi, C. Shen, F. Li, C. Ma, M. Huang, Z. Wang, J. Li, Environ. Pollut. 251 (2019) 72–80.
- [37] C. Xu, P. Zhang, L. Yan, J. Raman Spectrosc. 32 (2001) 862–865.
- [38] C. Dong, Z. Gao, Y. Li, M. Peng, M. Wang, Y. Xu, C. Li, M. Xu, Y. Deng, X. Qin, F. Huang, X. Wei, Y.G. Wang, H.Y. Liu, W. Zhou, D. Ma, Nat. Catal. 5 (2022) 485–493.
- [39] X. Song, N. Li, H. Zhang, L. Wang, Y. Yan, H. Wang, L. Wang, Z. Bian, ACS Appl. Mater. Interf. 12 (2020) 17519–17527.
- [40] W. Chen, P. Westerhoff, J.A. Leenheer, K. Booksh, Environ. Sci. Technol. 37 (2003) 5701–5710.